Distinct fission signatures predict mitochondrial degradation or biogenesis

Tatjana Kleele, Timo Rey, Julius Winter, Sofia Zaganelli, Dora Mahecic, Hélène Perreten Lambert, Francesco Paolo Ruberto, Mohamed Nemir, Timothy Wai, Thierry Pedrazzini, et al.

ARTICLE NATURE

Distinct fission signatures predict mitochondrial degradation or biogenesis

Tatjana Kleele[1], Timo Rey[1], Julius Winter[1], Sofia Zaganelli[1], Dora Mahecic[1], Hélène Perreten Lambert[1], Francesco Paolo Ruberto[2], Mohamed Nemir[2], Timothy Wai[3], Thierry Pedrazzini[2] and Suliana Manley[1]

[1] Institute of Physics, École Polytechnique Fédérale de Lausanne (EPFL), Route Cantonale, 1015 Lausanne, Switzerland

[2] Experimental Cardiology Unit, Department of Cardiovascular Medicine, University of Lausanne Medical School, 1011 Lausanne, Switzerland

[3] Mitochondrial Biology Group, Institut Pasteur, CNRS UMR 3691, Paris, France

Correspondence should be addressed to

T.K. (tatjana.kleele@epfl.ch)

S.M. (suliana.manley@epfl.ch)

Laboratory of Experimental Biophysics
École polytechnique fédérale de Lausanne
Rt de la Sorge 15
CH- 1025 Lausanne

Mitochondrial fission is a highly regulated process which, when disrupted, can alter metabolism, proliferation and apoptosis[1–3]. Dysregulation has been linked to neurodegeneration[3,4], cardiovascular disease[3] and cancer[5]. Key components of the fission machinery include the endoplasmic reticulum (ER)[6] and actin[7], which initiate constriction before dynamin-related protein 1 (Drp1)[8] binds to the outer mitochondrial membrane via adaptor proteins[9–11], to drive membrane scission[12]. In the mitochondrial life cycle, fission enables both biogenesis of new mitochondria and clearance of dysfunctional mitochondria via mitophagy[1,13]. Current models of fission regulation cannot explain how those dual fates are decided. However, uncovering fate determinants is challenging, since fission is unpredictable, and mitochondrial morphology is heterogeneous, with ultrastructural features below the diffraction limit. Thus, we used live-cell structured illumination microscopy (SIM) to capture mitochondrial dynamics. By analysing hundreds of fissions in Cos-7 cells and mouse cardiomyocytes, we discovered two functionally and mechanistically distinct types of fission. Mitochondria divide peripherally to shed damaged material into smaller daughter mitochondria destined for mitophagy, whereas healthy mitochondria proliferate via midzone division. Both types are Drp1-mediated, but ER- and actin-mediated pre-constriction and the adaptor Mff only govern midzone fission. Peripheral fissions are preceded by lysosomal contacts, and regulated by Fis1. These distinct molecular mechanisms explain how cells independently regulate fission leading to distinct mitochondrial fates.

Mitochondrial fission site positioning

Qualitatively, fission appears to occur randomly along the length axis of mitochondria (**Fig. 1a**). We recorded spontaneous mitochondrial dynamics at high temporal and spatial resolution, without pharmacological induction. Live-cell SIM imaging of Cos-7 cells allowed us to precisely determine the position of fission for mitochondria of diverse shapes and lengths (**Fig. 1b**, **Supplementary Video 1**). Analyzing hundreds of spontaneous fission events revealed a non-uniform probability distribution; instead, fission locations are bimodally distributed along a mitochondrion's relative length (**Fig. 1c**). We term these either "peripheral" (positioned less than 25% from a tip) or "midzone" division

(positioned within the central 50%). Considering mitochondrial area instead of length yielded similar results (**Extended data Fig. 1a, b**), as expected because of the relatively constant mitochondrial diameter. We observed this distribution, independent of the length of the dividing mitochondria (**Extended Data Fig. 1c, d**). As a consequence of this bimodality, smaller daughter mitochondria derived from peripheral divisions have a relatively narrow length distribution (1-2 μm) (**Extended Data Fig. 1e**). Mitochondria labelled with either inner or outer membrane markers revealed similar bimodal distributions, confirming complete fission (**Extended Data Fig. 1f**). To test whether our observations can be generalized, we measured fissions in postnatal mouse cardiomyocytes (**Fig. 1d**, **Supplementary Video 2**). Again, we recovered a bimodal distribution with mitochondria dividing either in the midzone or peripherally (**Fig. 1e**).

Dysfunction precedes peripheral fission

We wondered whether geometrically distinct fission types reflected underlying physiological differences. Mitochondria are hubs for metabolic functions, characterized by distinct physiological and biochemical properties. The potential across the inner membrane drives oxidative phosphorylation, creating a pH difference between matrix and intermembrane spaces. Reactive oxygen species (ROS), a toxic byproduct of oxidative phosphorylation, can lead to mitochondrial damage, often accompanied by membrane potential loss and Ca^{2+} and cytochrome c release[14]. We investigated the physiological states preceding mitochondrial fission with fluorescent sensors and live-cell SIM (**Fig. 1 f-i**). We found mitochondrial membrane potential as reported by the dye TMRE was reduced prior to fission in small peripheral daughter mitochondria (**Fig. 1f, g**, **Supplementary Video 3**) compared with corresponding large daughter mitochondria or non-dividing mitochondria. In contrast, no differences were observed between daughter mitochondria from midzone fissions. Similarly, the genetically encoded pH sensor SypHer reported a reduced matrix pH in small daughter mitochondria prior to fission (**Extended Data Fig. 2c, d**, **Supplementary Video 4**). Small peripheral daughter mitochondria containing mito-GFP maintained their intensity; thus, these results cannot be explained by their reduced volume (**Extended Data Fig. 2j, k**). Furthermore, the smallest mitochondria derived from midzone fission are similar in size to those from peripheral fissions (**Extended data Fig. 2c- i**).

Another indication of mitochondrial dysfunction is ROS accumulation, usually eliminated by anti-oxidative enzymes[15]. ROS levels measured by MitoSox (**Fig. 1h, i**) and genetically encoded mito-Grx1-roGFP sensors (**Extended Data Fig. 2l, m**) were elevated compared to non-dividing mitochondria or daughters from midzone fissions. Cells treated with 500 nM of the ROS scavenger MitoQ exhibited reduced peripheral fission rates, while midzone fission rates were unaffected (**Extended Data Fig. 2f**). Finally, we examined mitochondrial Ca^{2+} levels, with the genetically encoded sensors mito-R-Geco (**Extended Data Fig. 2n, o**, **Supplementary Video 5**) and Cepia3-mt (**Extended Data Fig. 2p, q)**. Mitochondrial Ca^{2+} plays important roles in cell survival and death by balancing homeostasis[16]. Ca^{2+} levels increased significantly in small peripheral daughter mitochondria, and mildly in large daughter mitochondria, compared with midzone or non-dividing mitochondria. Thus, we found no differences in the physiological states of midzone fissions before or after fission, whereas peripheral fission is preceded by a rise Ca^{2+} and in ROS, and reduced membrane potential and pH.

Distinct positions, distinct fates

Since the physiology of individual mitochondria showed signs of stress and damage upstream of peripheral fission, we hypothesized that it could be linked to degradation, whereas midzone fission could serve biogenesis. To test this, we analyzed the distribution of mitochondrial DNA (mtDNA) in Cos-7 cells stained with the vital dye PicoGreen (**Fig. 2a, b**, **Extended Data Fig. 3a)**. On average, there was no significant difference in the total number of mtDNA foci (nucleoids) in peripherally versus centrally dividing mitochondria. However, we observe that 32% of smaller daughter mitochondria from peripheral fissions contain no nucleoids, versus 3% from midzone fissions. Mitochondria lacking mtDNA also had diminished membrane potential compared to those containing mtDNA (**Extended Data Fig. 3b**). We observed similar results for mitochondrial RNA granules (MRGs, **Extended Data Fig. 3c-e**), which are composed of mtRNA and RNA processing proteins[17]. Daughter mitochondria arising from midzone fissions contained an elevated number of replicating (Mito-Twinkle positive) nucleoids compared to non-dividing mitochondria, consistent with a proliferative role (**Fig. 2c, d, Extended Data Fig. 3f**). In contrast, 75% of smaller peripheral daughter mitochondria contained no Twinkle foci. We then induced mtDNA damage by exposing cells to UV light (**Fig. 2e, f**), and labelled

newly synthesized RNA with Bromo-Uridine (BrU). Indeed, mitochondria have fewer BrU foci after UV treatment, indicating disruption of transcription (**Extended Data Fig. 3g**). Consistent with our hypothesis of their degradative role, the prevalence of nucleoids increased in small peripheral daughter mitochondria (82% versus 68% without UV irradiation).

We followed daughter mitochondria resulting from peripheral fissions, to discern their fates. Previous studies reported lysosome-mitochondria contacts prior to fission[18], which we observed in 92% of peripheral fissions, compared with only 13% of midzone fissions (**Fig. 2g, h**, **Supplementary Video 6**). At peripheral fission sites, we also observed mitochondrial-derived vesicles (MDVs), known to be targeted to late endosomes for degradation[19] (**Extended Data Fig. 6c, d**). Mitochondria undergoing peripheral fission also accumulated YFP-Parkin (**Fig. 2i, j**). These signatures link peripheral fission with mitophagy, the turnover of mitochondria by autophagy regulated by PINK1 and Parkin[20]. In some cases, we observed the uptake of small daughter mitochondria derived from peripheral fissions by autophagosomes (**Extended Data Fig. 3h**, **Supplementary Video 7**). To dissect the sequence of events leading to fission, we analyzed the timing of changes in mitochondrial physiology (**Extended Data Fig. 4**) and recruitment of the fission and autophagic machinery. This revealed that a drop in membrane potential, rise in Ca^{2+}, and recruitment of the autophagic machinery all precede peripheral fission. Changes in membrane potential and Ca^{2+} occur even before the inner mitochondrial membrane is significantly constricted (**Extended Data Fig. 4c**), suggesting a compartmentalization of the two daughter mitochondria prior to fission.

Previous studies established a paradigm whereby dividing mitochondria either re-fuse with the network, or remain isolated and undergo mitophagy[1]. Therefore, we followed the fate of daughter mitochondria after division. We found that small peripheral daughter mitochondria are excluded from further fusions or divisions in both Cos-7 cells (**Fig. 2k**) and primary mouse cardiomyocytes (**Extended Data Fig. 5a**), while the remaining daughter mitochondria regularly undergo further fission or fusion events.

Cell context dependent modulation

We wondered whether cells would be able to modulate each fission type independently, in a context-dependent manner (**Fig. 3a, b**). Thus, we subjected Cos-7 cells to metabolic stress by growing them in glucose-free (galactose supplemented) media. We observed that the rate of peripheral fissions per cell increased, whereas the rate of centrally dividing mitochondria remained constant (**Fig. 3a, Extended Data Fig. 5b**). A similar trend emerged in response to mtDNA damage induced by UV light. We also tested the effects of increased energy demand and hence oxidative stress on primary mouse cardiomyocytes, by treatment with isoproterenol, a non-selective β-adrenergic receptor agonist increasing contractility and inducing hypertrophy. We imaged cells after 48 h of stimulation and found increased rates of peripheral fissions compared to non-treated cells, while the rate of midzone fissions remained constant (**Fig. 3b, Extended Data Fig. 5c**). In contrast, when cells proliferate, our model predicts an upregulation of midzone fissions. To test this, we treated cardiomyocytes with a miR-199 mimic; indeed, we found increased rates of midzone fissions, whereas peripheral fission rates remain unchanged (**Fig. 3b, Extended Data Fig. 5d**). Thus, cellular stress and high energy demands, associated with oxidative damage, increase the rate of peripheral fissions, whereas cell proliferation, which requires biogenesis of new mitochondria, increases the rate of midzone fissions.

Distinct molecular machineries

The differences in physiology and fate of mitochondria derived from midzone versus peripheral fissions prompted us to investigate the molecular players involved. Previous studies report that mitochondrial-ER contacts[6], in coordination with actin polymerization[21], define division sites and trigger mitochondrial DNA replication upstream of Drp1. All fissions we observed were spontaneous, and mediated by Drp1 assembly (**Extended Data Fig. 6a, b**). We found that midzone fission sites consistently contacted the ER prior to fission, but most peripheral fission sites did not (**Fig. 3c, d**, **Extended Data Fig. 6h**, **Supplementary Video 8**). In accordance, immunostaining against PDZD8, a mitochondria-ER tethering protein[22], revealed a higher fluorescent signal at midzone fission sites (**Extended Data Fig. 6e, f**). This conditional involvement of ER contacts in midzone fissions lends insight to reports that not all fissions engage ER contacts (60-90%)[6,23] or include mtDNA replication (77%)[24]. Similarly, we found that actin consistently polymerized at midzone, but not peripheral fission sites (**Fig. 3e, f**). SiRNA of Inf2, a formin protein accelerating actin polymerization at the ER[21], led to

decreased rates of midzone fissions, while having no effect on peripheral fission rates (**Extended Data Fig. 6g and 7a**).

Several mitochondrial outer membrane proteins (Mff[9], Mid49/Mid51[10], Fis1[25]) regulate fission, but whether their roles are redundant or distinct remains unclear[11]. To investigate their roles in midzone versus peripheral fissions, we generated U2OS cell lines expressing endogenously tagged Mff-GFP or Fis1-GFP. Live-cell SIM revealed stark differences in the distribution of Mff and Fis1. Mff forms bright foci at constrictions leading to midzone fissions, and two-fold dimmer foci at peripheral fissions (**Fig. 3g, h**). In contrast, Fis1 does not show a punctate accumulation, decorating the outer membrane more evenly. However, we observed significant enrichment of Fis1-GFP on small daughter mitochondria from peripheral divisions (**Fig. 3i- j, Extended Data Fig. 6o**), consistent with its reported roles in mitophagy[26] and lysosome recruitment[18]. We observed similar distribution patterns of immunolabeled Mff and Fis1 in Cos-7 cells (**Extended Data Fig. 6i- l**), but did not find differences in accumulation of Drp1 adaptors Mid49/51 (**Extended Data Fig. 6m, n**). To quantify the distinct roles of Mff, Fis1 and Mid49/51, we measured peripheral and midzone fissions in wildtype and knock-out MEF lines[11] (Drp1$^{-/-}$, Mff$^{-/-}$, Fis1$^{-/-}$, Mid49$^{-/-}$/Mid51$^{-/-}$ dKO, Mff$^{-/-}$/ Mid49$^{-/-}$/Mid51$^{-/-}$ tKO; (**Fig. 3k, Extended Data Fig. 6p)**. While Drp1$^{-/-}$ MEFs show a global inhibition of fusion, Mff knock-out only reduces midzone fission rates, while conversely, Fis1 knock-out only reduces peripheral fission rates. We obtained similar results with siRNA mediated knock-down of Fis1 and Mff (**Extended Data Fig. 6q and 7b-d**). In contrast, cells depleted of Mid49 and Mid51 exhibit a 35% decrease in both peripheral and midzone fission rates, compared to wild-type cells. Thus, Mid49/51 is engaged in but not required for both types of fission.

To examine the implications of adaptor depletions, we studied their impact on cardiomyocyte response to perturbations. We induced contraction for 48 h in cardiomyocytes and subsequently quantified apoptosis in control and Fis1-depleted cells (**Fig. 3l, Extended Data Fig. 7e, f**). Indeed, 68% of stimulated cardiomyocytes lacking Fis1 underwent apoptosis (in contrast to 9-18% in control groups). Fis1 depletion also decreased proliferation rates, even in control conditions, perhaps due to disrupted mitochondrial quality control, which is linked to cell cycle arrest in cardiomyocytes[27]. Finally, we knocked down Mff in cardiomyocytes that were stimulated to proliferate. While miR-199 increased

cell proliferation in the control group, Mff-depleted cell proliferation rates were significantly reduced, in a dose-dependent manner (**Fig. 3m, Extended Data Fig. 7e, f**). This further highlights the importance of Mff-mediated midzone fissions for mitochondrial biogenesis during cell proliferation, and Fis-1 mediated peripheral fission for cell survival under stress conditions.

Discussion

Previous studies revealed that fission underlies both mitochondrial proliferation and degradation[1]. We discovered organelle-level regulation that reconciles this paradox, with the positioning of the fission site as a key morphological signature of the decision to proliferate or degrade. The formation of small daughter mitochondria to sequester damaged components has an advantage: such small mitochondria can be engulfed by autophagosomes, and allow the mass of degraded material to be minimized. Our fine spatiotemporal analyses of mitochondrial physiology revealed that the majority of peripheral divisions are preceded by decreased membrane potential and proton motive force, and elevated ROS and Ca^{2+} levels, well before the constriction by Drp1. While it is remarkable that a gradient forms within one mitochondrion, biological systems frequently use gradients to monitor their geometries[28], and even individual cristae can maintain different membrane potentials[29]. Thus, we speculate that peripheral fissions could use this gradient as a positioning cue, in the absence of extra-mitochondrial membrane contacts to define the location of the division site. This would explain how cells may regulate peripheral and midzone mitochondrial division independently, through intrinsic signals reflecting mitochondrial physiology.

Independent regulation is further supported by our observation that different adaptor proteins mediate peripheral and midzone fissions. Such a paradigm can account for the reported variability and seeming redundancy in the division machinery[30]. Mff accumulates at, and is only required for midzone fissions, while Fis1 is important for regulation of peripheral fission. Weaker Mff accumulation at poles and peripheral fission sites may be driven by curvature[6]. Initially, Fis1 was proposed to act as a Drp1 adaptor in yeast[31], but later studies in mammalian cells found no direct interactions with Drp1[11]. Indeed, we observe a global enrichment of Fis1 on the outer membrane of small, peripherally dividing mitochondria, rather than foci. Therefore, we propose that Fis1 does not act as Drp1 adaptor, but instead

regulates peripheral fission through the recruitment of lysosomes, consistent with findings that Fis1 recruits the lysosome-mitochondria tethering molecule TBC1D15[18].

The existence of two mechanistically and functionally distinct fission types has implications in the context of pathology. Excessive fission rates are a hallmark of diverse diseases[4,32], and its pharmacological inhibition has been proposed as potential therapy[33]. Other therapeutic approaches have aimed to stimulate mitochondrial biogenesis[34]. However, our model suggests that if under pathological conditions only one type of fission is dysregulated, treatment with global inhibitors may further disrupt cell homeostasis. Therefore, our findings indicate the potential for more rational and specific therapeutic targets.

REFERENCES

1. Twig, G. *et al.* Fission and selective fusion govern mitochondrial segregation and elimination by autophagy. *EMBO J.* **27**, 433–446 (2008).
2. Rambold, A. S., Kostelecky, B., Elia, N. & Lippincott-Schwartz, J. Tubular network formation protects mitochondria from autophagosomal degradation during nutrient starvation. *Proc. Natl. Acad. Sci. U S A* **108**, 10190–10195 (2011).
3. Song, M., Franco, A., Fleischer, J. A., Zhang, L. & Dorn, G. W. Abrogating Mitochondrial Dynamics in Mouse Hearts Accelerates Mitochondrial Senescence. *Cell Metab.* **26**, 872-883.e5 (2017).
4. Wang, W. *et al.* Parkinson's disease–associated mutant VPS35 causes mitochondrial dysfunction by recycling DLP1 complexes. *Nat. Med.* **22**, 54–63 (2016).
5. Ma, J.-T. *et al.* Effects of Dynamin-related Protein 1 Regulated Mitochondrial Dynamic Changes on Invasion and Metastasis of Lung Cancer Cells. *J. Cancer* **10**, 4045–4053 (2019).
6. Friedman, J. R. *et al.* ER Tubules Mark Sites of Mitochondrial Division. *Science* **334**, 358–362 (2011).
7. Ji, W., Hatch, A. L., Merrill, R. A., Strack, S. & Higgs, H. N. Actin filaments target the oligomeric maturation of the dynamin GTPase Drp1 to mitochondrial fission sites. *eLife* **4**, e11553 (2015).

8. Smirnova, E., Griparic, L., Shurland, D. L. & van der Bliek, A. M. Dynamin-related protein Drp1 is required for mitochondrial division in mammalian cells. *Mol. Biol. Cell* **12**, 2245–2256 (2001).
9. Gandre-Babbe, S. & van der Bliek, A. M. The Novel Tail-anchored Membrane Protein Mff Controls Mitochondrial and Peroxisomal Fission in Mammalian Cells. *Mol. Biol. Cell* **19**, 2402–2412 (2008).
10. Palmer, C. S. *et al.* MiD49 and MiD51, new components of the mitochondrial fission machinery. *EMBO Rep.* **12**, 565–573 (2011).
11. Osellame, L. D. *et al.* Cooperative and independent roles of the Drp1 adaptors Mff, MiD49 and MiD51 in mitochondrial fission. *J. Cell. Sci.* **129**, 2170–2181 (2016).
12. Fröhlich, C. *et al.* Structural insights into oligomerization and mitochondrial remodelling of dynamin 1-like protein. *EMBO J.* **32**, 1280–1292 (2013).
13. Burman, J. L. *et al.* Mitochondrial fission facilitates the selective mitophagy of protein aggregates. *J. Cell Biol.* **216**, 3231–3247 (2017).
14. Ashrafi, G. & Schwarz, T. L. The pathways of mitophagy for quality control and clearance of mitochondria. *Cell Death Differ.* **20**, 31–42 (2013).
15. Sturtz, L. A., Diekert, K., Jensen, L. T., Lill, R. & Culotta, V. C. A fraction of yeast Cu,Zn-superoxide dismutase and its metallochaperone, CCS, localize to the intermembrane space of mitochondria. A physiological role for SOD1 in guarding against mitochondrial oxidative damage. *J. Biol. Chem.* **276**, 38084–38089 (2001).
16. Mallilankaraman, K. *et al.* MICU1 Is an Essential Gatekeeper for MCU-Mediated Mitochondrial Ca2+ Uptake that Regulates Cell Survival. *Cell* **151**, 630–644 (2012).
17. Jourdain, A. A. *et al.* GRSF1 Regulates RNA Processing in Mitochondrial RNA Granules. *Cell Metab.* **17**, 399–410 (2013).
18. Wong, Y. C., Ysselstein, D. & Krainc, D. Mitochondria–lysosome contacts regulate mitochondrial fission via RAB7 GTP hydrolysis. *Nature* **554**, 382–386 (2018).
19. Soubannier, V., Rippstein, P., Kaufman, B. A., Shoubridge, E. A. & McBride, H. M. Reconstitution of Mitochondria Derived Vesicle Formation Demonstrates Selective Enrichment of Oxidized Cargo. *PLoS ONE* **7**, e52830 (2012).

20. Pickles, S., Vigié, P. & Youle, R. J. Mitophagy and Quality Control Mechanisms in Mitochondrial Maintenance. *Curr. Biol.* **28**, R170–R185 (2018).

21. Korobova, F., Ramabhadran, V. & Higgs, H. N. An Actin-Dependent Step in Mitochondrial Fission Mediated by the ER-Associated Formin INF2. *Science* **339**, 464–467 (2013).

22. Hirabayashi, Y. *et al.* ER-mitochondria tethering by PDZD8 regulates Ca^{2+} dynamics in mammalian neurons. *Science* **358**, 623–630 (2017).

23. Murley, A. *et al.* ER-associated mitochondrial division links the distribution of mitochondria and mitochondrial DNA in yeast. *eLife* **2**, e00422 (2013).

24. Lewis, S. C., Uchiyama, L. F. & Nunnari, J. ER-mitochondria contacts couple mtDNA synthesis with mitochondrial division in human cells. *Science* **353**, aaf5549 (2016).

25. Yu, R., Jin, S.-B., Lendahl, U., Nistér, M. & Zhao, J. Human Fis1 regulates mitochondrial dynamics through inhibition of the fusion machinery. *EMBO J.* **38**, e99748 (2019).

26. Xian, H., Yang, Q., Xiao, L., Shen, H.-M. & Liou, Y.-C. STX17 dynamically regulated by Fis1 induces mitophagy via hierarchical macroautophagic mechanism. *Nat. Commun.* **10**, 2059 (2019).

27. Kimura, W. *et al.* Redox Signaling in Cardiac Renewal. *Antioxid. Redox Signal.* **21**, 1660–1673 (2014).

28. Chang, F. & Minc, N. Electrochemical Control of Cell and Tissue Polarity. *Annu. Rev. Cell Dev. Biol.* **30**, 317–336 (2014).

29. Wolf, D. M. *et al.* Individual cristae within the same mitochondrion display different membrane potentials and are functionally independent. *EMBO J* **38**, (2019).

30. Koirala, S. *et al.* Interchangeable adaptors regulate mitochondrial dynamin assembly for membrane scission. *Proc. Natl. Acad. Sci. U S A* **110**, E1342–E1351 (2013).

31. Mozdy, A. D., McCaffery, J. M. & Shaw, J. M. Dnm1p GTPase-mediated mitochondrial fission is a multi-step process requiring the novel integral membrane component Fis1p. *J. Cell Biol.* **151**, 367–380 (2000).

32. Song, W. *et al.* Mutant huntingtin binds the mitochondrial fission GTPase dynamin-related protein-1 and increases its enzymatic activity. *Nat. Med.* **17**, 377–382 (2011).

33. Guo, X. *et al.* Inhibition of mitochondrial fragmentation diminishes Huntington's disease–associated neurodegeneration. *J. Clin. Invest.* **123**, 5371–5388 (2013).

34. Zamora, M., Pardo, R. & Villena, J. A. Pharmacological induction of mitochondrial biogenesis as a therapeutic strategy for the treatment of type 2 diabetes. *Biochem. Pharmacol.* **98**, 16–28 (2015).

FIGURE LEGENDS

Fig. 1 | Mitochondrial fissions are bimodally positioned and linked to distinct physiologies. a, Gallery of mitochondria one frame before division from SIM movies, binarized. **b**, Time-lapse SIM sequence of a peripheral and midzone fission of mitochondria (Mitotracker green). **c**, Histogram of fission positions relative to the total mitochondrial length (n=1393 fissions pooled from multiple data sets). Fissions occurring near the tip (orange, 0-25%) are termed 'peripheral'; those near the center (green, 25-50%) are termed 'midzone'. **d**, iSIM of mitochondria (Mitotracker green) in primary mouse cardiomyocytes. Insets: time-lapse sequences from indicated boxes. **e** Histogram of the relative position of fission in cardiomyocyte mitochondria (n=381 fissions), as in **c**. **f**, Mitochondrial membrane potential before and after a peripheral or midzone fission from SIM movies of TMRE-stained mitochondria. **g**, Normalized TMRE intensity as a function of relative position of fission, measured immediately before fission (n=56 fissions). **h** MitoSox labelling reveals ROS levels before and after a peripheral or midzone fission. **i**, Normalized MitoSox intensity as a function of relative fission position, measured immediately before fission (n=52 fissions). In **(g)**, **(i)**, circles indicate individual measurements; line: mean, bounds of box: 25th and 75th percentile; whiskers: min/max values, light blue area indicates mean intensity in non-dividing mitochondria (±SD). Scale bars are 0.5 μm in **b, f, h** and 10 μm in **d**. Arrows indicate fission sites. All panels excluding **(d)** and **(e)** show data from Cos-7 cells. *P< 0.05, **P<0.01, ***P<0.001. Number of experiments, statistical tests and exact P-values are provided in Supplementary Table 1.

Fig. 2 | Midzone and peripheral fissions differ in mtDNA content and fates. a, Mitochondria (mito-RFP, greyscale) and mtDNA (PicoGreen, green) before and after fission. **b**, Linear density of nucleoids as a function of fission position, individual data points (left) and violin plots (right) for binned groups (n=78 fissions). **c**, Replicating nucleoids (mito-Twinkle-GFP) and **d**, linear density, as in (**b)** (n=74 fissions). **e**, mtDNA and **f**, linear density after UV irradiation, as in (**b)** (n= 62 fissions). **g**, Mitochondria (mito-RFP, greyscale) and lysosomes (Lamp1-mEGFP, green) before and after peripheral or midzone fission. **h**, Position of fission in divisions contacting lysosomes or not prior to fission (n= 104 fissions). **i**, Mitochondria (mito-RFP, greyscale) and pre-mitophagic marker (YFP-Parkin, red) before and after fission. **j**, Pre-fission YFP-Parkin fold-change in intensity as a function of fission position. (n=34). **k**, Schema depicting the fates of daughter mitochondrion from peripheral and midzone fissions. Mitochondria tracked for >100 s post-fission were included. Numbers in parenthesis are total numbers of events. All panels show data from Cos-7 cells, and circles indicate individual measurements. In panels **(b)**, **(d)**, **(f)**, the blue line represents mean mtDNA density. In **(j)**, line: mean, bounds of box: 25th and 75th percentile; whiskers: min/max values, light blue area indicates mean intensity in non-dividing mitochondria (±SD).. Scale bars are 0.5 μm. White arrowheads indicate fission sites. ***P<0.001. Number of experiments, statistical tests and exact P-values are provided in Supplementary Table 1.

Fig. 3 | Midzone and peripheral fissions are independently regulated by distinct molecular machineries. a, Peripheral (orange) and midzone (green) fission rates in control, starved, or UV-exposed Cos-7 cells (n≥ 15 FOV per group). **b**, Fission rates in postnatal mouse cardiomyocytes in control, stimulated, or proliferation induced cells (n≥ 19 FOV per group). **c**, SIM of mitochondria (mito-GFP, grey) and ER (KDEL-RFP, magenta) before a peripheral or midzone fission. **d**, Position of fission in mitochondria contacting the ER (left) or not (right) prior to fission (n= 93 fissions) in Cos-7 cells. **e**, SIM of mitochondria (mito-GFP, grey) and actin (Ftractin-Apple, yellow) before peripheral and midzone fissions. **f**, Fission position in mitochondria that accumulate actin (left) or not (right) prior to fission (n=80 fissions). **g**, SIM of mitochondria (Mitotracker red, grey) in U2OS cells endogenously expressing Mff-GFP for a peripheral and midzone fission. **h**, Mff-GFP fold-change in intensity at the

fission site of peripheral and midzone divisions (n= 54 fissions). **i**, SIM of mitochondria (Mitotracker red, grey) in U2OS cells endogenously expressing Fis1-GFP (green) for a peripheral and midzone fission. **j**, Fis1-GFP fold-change in intensity over the surface of daughter mitochondrion before fission (n= 35 fissions). **k**, Peripheral (orange) and midzone (green) fission rates in wild-type, *Drp1*$^{-/-}$, *Mff*$^{-/-}$, *Fis1*$^{-/-}$, *Mid49*$^{-/-}$/*Mid51*$^{-/-}$ dKO, stained with Mitotracker green (n≥ 15 cells per group). **l**, Percentage of apoptotic (Caspase 3/7 positive) cardiomyocytes in control, Fis1 and Mff depleted cells +/- stimulation with Isoproterenol (n>29 FOV per group). **m**, Percentage of proliferating (EdU positive) cardiomyocytes in control, Mff and Fis1 depleted cells +/- treatment with miR-199 (n≥49 FOV per group). In **(a)**, **(b)**, **(h), (j), (k)** line: mean, bounds of box: 25th and 75th percentile; whiskers: min/max values, circles: individual measurements. Number of experiments, statistical tests and exact P-values are provided in Supplementary Table 1.; n.s. P>0.05, *P<0.05, **P<0.01, ***P<0.001. Scale bars are 0.5 μm. Constriction sites are indicated by white arrowheads.

METHODS

No statistical methods were used to predetermine sample size. For studies involving multiple experimental conditions, studies were performed on cells originated from the same cell line batch and randomly assigned to experimental conditions.

Plasmids and reagents

Mito-GFP (Cox-8 presequence) was a gift from Hari Shroff (NIH, Bethesda), mCherry-Drp1 and BFP-KDEL were gifts from Gia Voeltz (Addgene, plasmid #49152 and #49150)[1], SypHer mt was a gift from Nicolas Demaurex (Addgene plasmid #48251)[2], pLPCX mito Grx1-roGFP2 was a gift from Tobias Dick (Addgene plasmid #64977)[3], pCMV Cepia3mt was a gift from Masamitsu Iino (Addgene plasmid #58219)[4], Lamp1-GFP was a gift from Ron Vale (Addgene plasmid #16290)[5], YFP-Parkin was a gift from Richard Youle (Addgene plasmid #23955)[6] and EGFP-LC3 was a gift from Karla Kirkegaard (Addgene plasmid #11546)[7], CMV-mito-R-GECO1 was a gift from Robert Campbell (Addgene plasmid #46021)[8]. FASTKD2-eGFP and mito-Twinkle-eGFP[9] were gifts from Jean-Claude Martinou. Ftractin-Apple was a gift from Henry N. Higgs (Dartmouth College, Hanover), Mito-tagRFP was

amplified from Mito-GFP. Wild-type, Drp1$^{-/-}$, Mff$^{-/-}$, Fis1$^{-/-}$, Mid49$^{-/-}$/Mid51$^{-/-}$ dKO, Mff$^{-/-}$/ and Mid49$^{-/-}$/Mid51$^{-/-}$ tKO mouse embryonic fibroblasts where a gift from Mike Ryan and have previously been described[10].

The stable FASTKD2-eGFP cell line was recently described[11]. In brief, co-transfection of HEK293T cells with pWPT_FASTKD2-eGFP and packaging plasmids pMD2.G and psPAX2 was achieved using calcium phosphate precipitation. Medium containing virus was collected 48 h after transfection and filtered using membranes with a pore size of 0.45 μm. The viral supernatant and polybrene were added to 70% confluent recipient cells. FACS sorting was performed to select for cells expressing GFP.

Oligonucleotides for siRNA were made by Microsynth to knock down Mff (sense strand 5'-CGC UGA CCU GGA ACA AGG A-dTdT-3′), Fis1 (sense strand 5′-CGA GCU GGU GUC UGU GGA G-dTdT-3) and INF2 (sense strand 5'-GCA GUA CCG CUU CAG CAU UGU CAT T-3' and 5'-GGA UCA ACC UGG AGA UCA UCC GCT T-3'). siRNA transfection was performed using Lipofectamine RNAi Max (Invitrogen) and cells were imaged 72 h after transfection.

The following reagents were also used: Mitotracker Green ((ThermoFisher M7514), Mitotracker Red FM ((ThermoFisher M22425), Tetramethylrhodamine ethyl ester perchlorate (Sigma, 87917), MitoSOX™ Red Mitochondrial Superoxide Indicator (Thermo Fisher M36008), Mitoquinol 98% (Adipogen SA CAY-89950-10), Quant-iT PicoGreen (Life Technologies P7581), CellEvent Caspase-3/7 (Life Technologies C10723), Fis1 polyclonal antibody (Proteintech 109561-AP), Mff (C2orf33) polyclonal antibody (Life Technologies PA567357), PDZD8 polyclonal antibody (Life Technologies PA553368), Mid49 (SMCR7) polyclonal antibody (Life Technologies, PA559950), TOM20 mouse monoclonal antibody (Santa Cruz sc-17764) and Alexa fluorophore-conjugated secondary antibodies from Life Technologies.

Generation of knock-in U2OS cells

Crispr/Cas9-mediated knock-in of EGFP into the MFF locus directly upstream of the start codon was performed using a plasmid encoding EGFP 2 flanked by 729 bp of upstream and 723 bp of downstream homologous DNA sequence cloned into pEX-A258 to create plasmid pTW343 (pEX-

A258-eGFP_hMFF_Template KI). Two pairs of sgDNA targeting MFF (sgDNA1: forward 5'-aaacAGTGATGTGTCACTGCTTGTC-3' and reverse 5' CACCGACAAGCAGTGACACATCACT-3', sgDNA2: forward 5'- CACCGCATTTAAATACAGTAAATAC and reverse 5'-aaacGTATTTACTGTATTTAAATGC-3') were cloned into pSpCas9n(BB)-2A-Puro (PX462) V2.0 (a gift from Feng Zhang (Addgene plasmid # 62987)[12].

Crispr/Cas9-mediated knockin of EGFP into the FIS1 locus directly upstream of the start codon was performed using a plasmid encoding EGFP 2 flanked by 721 bp of upstream and 624 bp of downstream homologous DNA sequence cloned into pEX-A258 to create plasmid pTW343 (pEX-A258-eGFP_hFIS1_Template KI). Two pairs of sgDNA targeting FIS1 (sgDNA1: forward 5'-CACCGCTGAACGAGCTGGTGTCTG-3' and reverse 5' aaacCAGACACCAGCTCGTTCAGC-3', sgDNA2: forward 5'- CACCGCTCGTTCAGCACGGCCTCCA and reverse 5'-aaacTGGAGGCCGTGCTGAACGAGC-3') were cloned into pSpCas9n(BB)-2A-Puro (PX462) V2.0 (a gift from Feng Zhang (Addgene plasmid # 62987). To knock in eGFP into either the MFF or FIS1 loci, U2OS cells were co-transfected with pSpCas9n(BB)-2A-Puro (PX462) V2.0 constructs carrying the appropriate sgDNA sequences and linearized Template plasmids (pTW343 for hMFF and pTW344 for hFIS1) using Lipofectamine 2000. 24 h after transfection, GFP-positive cells were individually isolated by fluorescence-activated cell sorting. Clones were expanded and were validated by PCR genotyping of genomic DNA and fluorescent imaging.

Cell culture and transfection

Cos-7 cells were grown in Dulbecco's modified Eagle medium (DMEM) supplemented with 10% fetal bovine serum and maintained in culture for a maximum of 20 passages or Galactose supplemented medium[13]. 10-24 h prior to transfection, cells were plated on 25 mm glass cover slips (Menzel, #1.5) at 1×10^5 cells ml^{-1}. Plasmid transfections were performed with 1.5 µl Lipofectamine 2000 (Invitrogen) per 100 µL Opti-MEM media (Invitrogen). The following amounts of DNA were transfected per ml: 150 ng Mito-GFP, 250 ng Mito-tagRFP, 100 ng Drp1-mCherry, 300 ng Tom20-RFP, 400 ng Mito-SypHer, 400 ng Grx1-roGFP2, 150 ng Mito-R-Geco, 400 ng Cepia3-mt, 350 ng

KDEL-RFP, 250 ng, Lamp1-GFP, 350 ng, EGFP-LC3, 400 ng YFP-Parkin and 200 ng MitoTwinkle-GFP. Cells were imaged the next day.

Primary mouse cardiomyocyte culture

Cardiac myocytes were prepared from ventricles of P1 neonatal mice using Pierce Cardiomyocyte Isolation Kit (Life Technologies 88281) following manufacturer's instructions. After digestion, the adherent non-myocyte cells were removed by pre-plating in 10cm tissue culture plates for 45 min. The non-adherent cardiomyocytes were seeded in complete Cardiomyocyte plating medium supplemented with 10% fetal calf serum and antibiotics at a density of 4-5 X 105 cells/well on Poly-L-Lysine (Sigma P-7890) and Gelatin (Sigma G9891)-coated coverslips in 6-well plates. To stimulate contraction, 24h post-plating the cardiomyocytes were fed with fresh medium supplemented with 2% FCS and with 10-5 M Isoproterenol (Sigma I-2760). To induce proliferation, cardiomyocytes were transfected with 50 nM miR-199 mimic[14] (Pharmacon, miRIDIAN Mimic Has-miR-199a-3p; C300535-05) using Lipofectamine RNAi-Max following manufacturer's instructions (Life Technologies, 13778). Cardiomyocytes were observed 48 post-treatment or transfection.

Western blotting

For immunoblots 48-72 h after siRNA transfection, Cos-7 cells were lysed in RIPA buffer (Sigma) supplemented with fresh proteases inhibitors (Sigma Aldrich 11836170001) on ice for 30 min. A centrifugation at 16,000 g for 10 min at 4˚C was performed to remove the insoluble material. Protein concentrations were determined using a Pierce BCA protein assay kit (Life Technologies, 23227) and equal amounts of protein were analyzed by self-casted 7.5 or 15% SDS-PAGE (30-50 µg of proteins per lane). For immunoblotting, proteins were transferred to nitrocellulose membranes (BioRad) electrophoretically and incubated with the specified primary antibodies (see above), diluted in 5% non-fat dry milk in Tris buffered saline with Tween 20 (TBST). The blots were further incubated with anti-rabbit or anti-mouse HRP conjugated secondary antibodies (GE Healthcare) and visualized using ECL (GE Healthcare). Where required, images of Western blotting were treated for contrast enhancement and densitometric analyses were performed using ImageJ.

Primary antibodies used for Western blot

The following primary antibodies were used for Western blots: anti-Fis1 (LuBioScience GmbH, 10956-1-AP, diluted 1:2000), anti-Mff (Life Technologies, PA5-52765, diluted 1:500-1:1000), anti-Inf2 (Sigma-Aldrich HPA000724, diluted 1:2000), anti-alpha-Tubulin (Santa Cruz sc-5286, diluted 1:2000).

RT-PCR

Total RNA was extracted from neonatal cardiomyocytes 48h post transfection using the miRNeasy® Mini Kit (Qiagen, #1038703). An optional step of DNAse (Qiagen #79254) digestion was performed following manufacturer protocol. cDNA was synthesized from 1ug total RNA using the PrimeScript RT-PCR Kit (Takara #RR014B) and Syber Green qRT-PCR was performed on Quantstudio 12k (Life technology) using the SYBR Green PCRmix (Applied Biosystems, #43676589). For SYBR Green qRT-PCR, 4ul of cDNA (25ng/ul) were mixed with 5ul of Power Sybr® PCR Master Mix, 0.5ul of Forward Primer (5 uM) and 0.5ul of Reverse Primer (5 uM). The cDNA mix was incubated 2 min at 50°C followed by a denaturation step of 2 min at 95°C and an amplification step of 40 cycles at 95°C for 15 sec and at 60°C for 45 sec.

Fis1 forward primer 5'-CCGGCTCAAGGAATATGAAA-3'
Fis1 reverse primer 5'-ACAGCCAGTCCAATGAGTCC-3'
Mff forward primer 5'-AGTGTGATAATGCAAGTCCCAGA-3'
Mff reverse primer 5'-GAGTGGACTGGATAAGGTCAAGA-3'
Gapdh forward primer 5'-TGCACCACCAACTGCTTAGC-3'
Gapdh reverse primer 5'-GGCATGGACTGTGGTCATGAG-3'

Live-cell treatments

TMRE: Cells were incubated with 500 nM TMRE for 10 min followed by rinsing in PBS.

Mitotracker: Cells were incubated in 500 nM Mitotracker for 5 min followed by rinsing in PBS.

PicoGreen: to image mtDNA, cells were stained with PicoGreen diluted 1:500 for 20 min.

MitoSox: Cells were incubated with 5uM MitoSox for 2-4 h prior to imaging.

MitoQ: Cells were incubated with 500nM MitoQ[15] for 30-45 min prior and during imaging following the manufacturer's instructions and a fresh aliquots were made every day.

Bromouridine tagging of RNA

Cos-7 cells were incubated with 5 mM 5-bromouridine (BrU) in complete culture medium for 1 h before fixation, as described previously[12]. BrU was stored at −20 °C, and heated and vortexed before use. Samples were immunolabeled with anti-bromodeoxyuridine (BrdU) (Roche 11170376001; 1:250 to 1:500 dilution) to visualize BrU signal.

SIM imaging

Single and dual-color SIM imaging was performed on an 3D NSIM Nikon inverted fluorescence microscope (Eclipse Ti; Nikon) equipped with an electron charge coupled device camera (iXon3 897; Andor Technologies). The microscope was equipped with a 100x 1.49 NA oil immersion objective (CFI Apochromat TIRF 100XC Oil; Nikon). Live-cell imaging was performed at 37°C using a 488 and 561 nm laser. Acquisition setting were adapted to yield the best image quality with minimal photobleaching (laser power 0.5-15%, Exposure time 30-100 ms). Images were captured using NIS elements software (Nikon) at temporal resolution of 1 s for single-color and 6-8 s for dual-color imaging. Imaging was performed at 37˚C in pre-warmed Leibovitz medium. Each sample was imaged for a maximum of 90 min.

Instant SIM (iSIM),

Single and dual color instant SIM imaging was performed on a custom-built microscope setup as previously described[16,17]. Fluorescence was collected with a 1.49 NA oil immersion objective (APONXOTIRF; Olympus), with 488 nm and 561 nm excitation lasers and an sCMOS camera (PrimeBSI, 01-PRIME-BSI-R-M-16-C, Photometric). Images were captured at 0.5-5 s temporal resolution for both channels. All imaging was performed at 37˚C in Leibovitz media. Raw iSIM images were subsequently deconvolved using the Lucy-Richardson deconvolution algorithm[18] provided by Hari Shroff implemented in MATLAB, and were run for 40 iterations.

Confocal imaging

Ratio-metric imaging of Grx1-rGFP was performed on an inverted microscope (DMI 6000; Leica) equipped with hybrid photon counting detectors (HyD; Leica). The sample was excited

sequentially frame by frame with 408 nm and 488 nm with the detection set to 500-535 nm. Fluorescence was collected through a 63x 1.40 NA oil immersion objective (HC PL APO 63x/1.40 Oil CS2; Leica). Images were captured using the LAS X software (Leica). All imaging was performed at 37˚C in pre-warmed Leibovitz medium for maximum 90 min per sample.

For confocal microscopy of fixed BrU samples the imaging was performed using a Leica TCS SP8 inverted microscope equipped with 405-, 488-, 552- and 638-nm lasers and a Plan-Apochromat oil objective (×63, NA 1.4). The Lightning mode (Leica) to generate deconvolved images. Microscope acquisitions were controlled by LAS X (v. 3.5.2) software from Leica.

CLEM and Caspase 3/7 samples were imaged on a Zeiss LSM 700 inverted confocal microscope with equipped with a Plan-Apochromat oil objective (×63, NA 1.40) and 488-nm and 555-nm solid-state lasers and three photomultipliers. Acquisitions were controlled by the Zeiss Zen (v. 6.0.0) software.

Immunofluorescence

Cells were seeded on glass cover slips and grown to a confluence of ~80%. Fixation of cultured cells was performed in cold 4% paraformaldehyde (PFA) in phosphate-buffer saline (PBS) for 20 min, then cells were washed 3x in PBS. Subsequently cells were incubated with 0.3% Triton X-100 and 1% pre-immune goat serum for 30 min. The same buffer was used to incubate cells with the specified primary antibody (see above) over night at 4°C. After washing in PBS, cells were incubated with the appropriate secondary antibody for 1h and rinsed in PBS before imaging.

Immunohistochemistry on cardiomyocytes

CMs (P1) were transfected with 25nM siFis1or siMff for 6 h and then transfected with 50 nM of Mir-199 mimic for 48h. EdU was added in fresh medium after 56 h and kept for the last 18 h. Cells were then fixed for 10 min in in 4% paraformaldehyde in PBS and permeabilized with 0.3% Triton X100 in PBS. After blocking (PBS containing 0.001% Triton X100, 1% BSA and 1% FCS), cells were incubated overnight at 4 °C with anti-TroponinI (1:500). The day after, cells were washed 3 times and incubated 1 h at RT in the dark with the secondary- conjugated antibody diluted 1:500 (488 goat anti-

rabbit A11008 Life Technology). EdU has been labelled and detected using a Click-iT EdU Alexa Fluor 594 Imaging Kit (Invitrogen C10339). Nuclei were stained with DAPI (Invitrogen).

Correlated confocal and TEM

Cells were seeded on gridded coverslips (MatTek, P35-1.5-14-CGRD-D) and grown to 50-60% confluence. Cells were fixed at room temperature for 1 h in freshly prepared fixative (2% PFA, 1% glutaraldehyde in PBS 0.1M, pH 7.4), followed by 10x washing in PBS. Samples were imaged by confocal microscopy on the same day and z-stacks were acquired of whole cells, the pinhole was closed to 0.5 AU and pixel size reduced to 50-100 nm in xy and 100-150 nm in z. Samples were stored overnight, in PBS at 4°C. They were then stained with osmium and potassium ferrocyanide, followed by osmium alone, each with cacodylate buffer. They were finally stained with 1% uranyl acetate, then washed in water, dehydrated through 15 increasing concentrations of alcohol, and infiltrated with Epon resin. This was polymerized over night at 65°C. Serial, ultra-thin serial sections were then cut of the cell of interest, and the sections collected on single slot copper grids with a formvar support membrane. Images were recorded in a transmission electron microscope operating at 80kV (FEI Company, Tecnai Spirit).

Image analysis

All image analysis was performed with the open-source ImageJ/Fiji[19,20] (including Weka Segmentation, EMBL bleach correction plugins). Mitochondrial fissions were defined as events, where a single mitochondrion divided into two independently moving daughter mitochondria in live-cells and in fixed cells when a (Drp1-positive) constrictions site showed a diameter of <180 nm, measured via FWHM across the constriction. For representation purpose, a 1 pixel Gaussian Filter was used and some videos where bleach corrected using bleach correction.

Relative position of constriction site: The positioning of constriction site was measured manually by drawing a line along the length axis of the mitochondrion in the frame before fission. For branched mitochondria (~13 % of mitochondrial population), the length of individual branches were summed.

Relative fluorescent intensity: Intensity measurements of biosensors were analyzed by measuring mean fluorescence intensity on each side of the constriction and in single daughter mitochondria after fission (ROI defined by using Otsu thresholding) on SIM images and subtracting the cytosolic background. For normalization, the mean fluorescence intensity was measured in three non-dividing mitochondria within the same field of view at the same time-point. For fixed samples (anti-PDZD8, anti-Mff, anit-Fis1, anti-Mid49), the mean intensity was measured in a 500 nm circle placed at the constriction site and normalized over the fluorescent signal along the non-constricted part of the mitochondrion. For measuring Drp1 , Lamp1-GFP, Mff-GFP and Fis1-GFP intensities, a 500 nm circle was placed at the constriction site and normalized over the intensity of at a 500 nm circle placed on a non-constricted part of the same mitochondrion.

Fission rate: To measure the fission rate, the total mitochondrial volume was calculated using trainable Weka segmentation (Fiji plugin) followed by binarization of the image. The total mitochondrial length was calculated using the total volume in the binarized image divided by the mean mitochondrial diameter. Fission rates were indicated as number of fissions occurring per μm length of mitochondria, per min.

ER or actin contacts: Contacts between mitochondria and ER or actin were measured by placing a line along the length axis of the mitochondrion crossing the constriction site and measuring the intensity profile for both channels. A contact site was defined, if the two signals cross at the constriction site (ER signal increases at least 2x over background) for at least three consecutive frames before fission.

Lysosome-mitochondria contact: A contact between mitochondria and lysosome was categorized as a close proximity (<500 nm) between lysosomes and the mitochondrial constriction site for at least three consecutive frames before fission.

BrU quantification: Individual cells were selected manually, using Fiji's rectangular selection tool. Three consecutive slices to focus at the bottom of the cell were then chosen upon inspection & foci were detected automatically in both BrU, and FASTKD2 channels using a fixed threshold. Foci that occurred in both channels were then counted as relevant mitochondrial RNA-transciption granules, whereas nuclear transcription for instance, was excluded from the analysis. Multiple thresholds were

tried, where 150 a.u. provided the most sensible results in control cells and are represented in Extended Data Fig. 3g, though all other data are provided in the source-data files, and followed the same trend. The same pipeline was applied to both Control and UV-treated samples.

Animal experiments

Mice were housed in a 12-hour light / 12-hour dark cycle at a temperature of 23oC with 40 to 60% humidity. All animal experiments were approved by the Government Veterinary Office (Lausanne, Switzerland) and performed according to the University of Lausanne Medical School institutional guidelines.

Statistics and Reproducibility

Sample sizes were determined on the basis of prior experience in previous experiments. All statistics were performed using OriginPro software. First, datasets were tested for normal distribution using D'Agostino-Pearson normality test (significance value of 0.05). If a dataset failed this test, a non-parametric test was chosen to compare significance of means between groups (Mann-Whitney test for two samples). For normally distributed datasets, a t-test was chosen to compare two samples. For a detailed description of statistical tests used and exact P-Values, please see **Supplementary Table 1**. Critical comparative datasets (Fis1 and Mff datasets, Drp1 intensity analysis, ER analysis) were partially re-analyzed or analyzed with an automated analysis pipeline to exclude observer bias. p values < 0.05 were considered to be significant and indicated by "∗"; p values < 0.01 were indicated by "∗∗" and <0.001 by "∗∗∗."

METHOD REFERENCES

1. Friedman, J. R. *et al.* ER Tubules Mark Sites of Mitochondrial Division. *Science* **334**, 358–362 (2011).
2. Poburko, D., Santo-Domingo, J. & Demaurex, N. Dynamic Regulation of the Mitochondrial Proton Gradient during Cytosolic Calcium Elevations. *J. Biol. Chem.* **286**, 11672–11684 (2011).
3. Gutscher, M. *et al.* Real-time imaging of the intracellular glutathione redox potential. *Nat. Methods* **5**, 553–559 (2008).

4. Suzuki, J. *et al.* Imaging intraorganellar Ca2+ at subcellular resolution using CEPIA. *Nat. Commun.* **5**, 4153 (2014).
5. Minin, A. A. *et al.* Regulation of mitochondria distribution by RhoA and formins. *Journal of Cell Science* (2006) doi:10.1242/jcs.02762.
6. Narendra, D., Tanaka, A., Suen, D.-F. & Youle, R. J. Parkin is recruited selectively to impaired mitochondria and promotes their autophagy. *J. Cell Biol.* **183**, 795–803 (2008).
7. Jackson, W. T. *et al.* Subversion of cellular autophagosomal machinery by RNA viruses. *PLoS Biol.* **3**, e156 (2005).
8. Wu, J. *et al.* Improved orange and red Ca^{2}± indicators and photophysical considerations for optogenetic applications. *ACS Chem. Neurosci.* **4**, 963–972 (2013).
9. Spelbrink, J. N. *et al.* Human mitochondrial DNA deletions associated with mutations in the gene encoding Twinkle, a phage T7 gene 4-like protein localized in mitochondria. *Nat. Genet.* **28**, 223–231 (2001).
10. Osellame, L. D. *et al.* Cooperative and independent roles of the Drp1 adaptors Mff, MiD49 and MiD51 in mitochondrial fission. *J. Cell Sci.* **129**, 2170–2181 (2016).
11. Rey, T. *et al.* Mitochondrial RNA granules are fluid condensates positioned by membrane dynamics. *Nat. Cell Biol.* **22**, 1180–1186 (2020).
12. Ran, F. A. *et al.* Genome engineering using the CRISPR-Cas9 system. *Nat. Protoc.* **8**, 2281–2308 (2013).
13. Marroquin, L. D., Hynes, J., Dykens, J. A., Jamieson, J. D. & Will, Y. Circumventing the Crabtree Effect: Replacing Media Glucose with Galactose Increases Susceptibility of HepG2 Cells to Mitochondrial Toxicants. *Toxicol. Sci.* **97**, 539–547 (2007).
14. Eulalio, A. *et al.* Functional screening identifies miRNAs inducing cardiac regeneration. *Nature* **492**, 376–381 (2012).
15. Kelso, G. F. *et al.* Selective targeting of a redox-active ubiquinone to mitochondria within cells: antioxidant and antiapoptotic properties. *J. Biol. Chem.* **276**, 4588–4596 (2001).
16. York, A. G. *et al.* Instant super-resolution imaging in live cells and embryos via analog image processing. *Nat. Methods* **10**, 1122–1126 (2013).

17. Mahecic, D. *et al.* Homogeneous multifocal excitation for high-throughput super-resolution imaging. *Nat. Methods* **17**, 726–733 (2020).
18. Holmes, T. J. & Liu, Y. H. Richardson-Lucy/maximum likelihood image restoration algorithm for fluorescence microscopy: further testing. *Appl. Opt.* **28**, 4930–4938 (1989).
19. Schindelin, J. *et al.* Fiji: an open-source platform for biological-image analysis. *Nat. Methods* **9**, 676–682 (2012).
20. Schneider, C. A., Rasband, W. S. & Eliceiri, K. W. NIH Image to ImageJ: 25 years of image analysis. *Nat. Methods* **9**, 671–675 (2012).

MAIN TEXT STATEMENTS

ACKNOWLEDGMENTS

We thank Cécilia Cottiny and Mariona Colomer for experimental and technical assistance, Mary-Claude Croisier and Graham Knott from the BioEM (EPFL) for carrying out the electron microscopy, Thierry Laroche (BIOP, EPFL) for imaging support and Mike Ryan for the MEF lines. We thank Thomas Misgeld, Jean-Claude Martinou and Pavan Ramdya for feedback on the manuscript. Research in S.M.'s lab is supported by the National Centre of Competence in Research Chemical Biology, the European Research Council (CoG 819823, Piko) and the Swiss National Science Foundation (182429). T.K. received funding from European Molecular Biology Organization (ALTF-739-2016) and the Munich Cluster for Systems Neurology (SyNergy). This work is supported in part by grants from the Swiss National Science Foundation to T.P. (no CRSII5_173738 and no 31003A_182322).

AUTHOR CONTRIBUTIONS

T.K. and S.M. conceived the project and designed experiments. T.K. performed imaging experiments and analysis. T.R. performed the Mito-Twinkle, FASTKD2, BrU and MitoSox imaging and contributed to the analysis. T.K. and J.W. performed the Caspase, Drp1 and LC3 imaging. D.M. developed and adjusted the iSIM setup. T.K., T.R. and D.M. performed the TEM experiments. S.Z.

performed the western blots. F.P.R., M.N. and T.P. designed and performed culturing of mouse cardiomyocytes and the proliferation assay. T.W., S.Z. and H.P.L. designed and cloned the Crispr/Cas9 transgenic lines. T.K. and S.M. designed figures and wrote the manuscript, with input from all authors.

CORRESPONDING AUTHOR

Correspondence and request for materials should be addressed to Tatjana Kleele (tatjana.kleele@epfl.ch) and Suliana Manley (suliana.manley@epfl.ch). Reprints and permissions information is available at www.nature.com/reprints

COMPETING INTERESTS

The authors declare no competing interest.

SUPPLEMENTARY INFORMATION:

Supplementary information is available for this paper (Extended Data Figures 1-7, Supplementary Figure 1, Supplementary Table 1 and Supplementary Videos 1-8).

DATA AND CODE AVAILABILITY STATEMENTS

Data and materials availability

All imaging as well as numerical data relevant to this study are publicly available on the online repository Zenodo (https://doi.org/10.5281/zenodo.3550643) or upon reasonable request. The data are organized according to their appearance in the main figures and extended data figures. Plasmids and cell lines are available to share, do not hesitate to contact the corresponding authors.

Code availability

The custom-written Fiji-macro script for BrU quantification is available at github.com/TimoHenry and the custom written Fiji-macro for Caspase staining is available at https://github.com/jutziw/mitochondrial_division.

EXTENDED DATA FIGURE LEGENDS

Extended Data Fig. 1 | Distribution of mitochondrial fission sites. a, Histogram of the relative position of constriction/fission measured by mitochondrial volume (n=190 fissions). The two peaks are colored in orange (0-25 bin; 'peripheral position') and green (25-50 bin; 'midzone position'). **b**, Relative position of mitochondrial fission measured by length versus measured by area (n=190 fissions) **c**, Stacked histogram of the relative position of fission for different bins grouped by the total length of the dividing mitochondria (n= 1393). **d**, Scatter plot of the total length of dividing mitochondria versus the relative position of the fission site along the length axis with peripheral fissions (0-25% bin) colored in orange and midzone fissions (25-50% bin) in green (n=1393 fissions). **e**, Length distribution of the smaller (light color) and larger (dark color) daughter mitochondria arising from peripheral left, orange) and midzone (right, green) fissions. **f**, Histogram of relative position of fission in datasets acquired with a mitochondrial inner membrane marker (left, Cox-8 targeting domain; n=510 fissions) and a mitochondrial outer membrane marker (right, TOM20; n=368 fissions).

Extended Data Fig. 2 | Physiological changes preceeding fission is independent of volume and absolute length.

a, Normalized mito-GFP intensity depending on the relative position of fission measured in mitochondria immediately before fission. (n= 50 fissions). **b**, Dependence on the length of the daughter mitochondria of normalized Mito-GFP intensity immediately before peripheral (orange) or midzone (green) fissions (n= 50 fissions). **c**, Dependence on the length of the daughter mitochondria of normalized TMRE intensity immediately before peripheral (orange) or midzone (green) fissions (n= 56 fissions). **d**, Dependence on the length of the daughter mitochondria of normalized mito-SypHer intensity before fission (n= 53 fissions). **e**, Dependence of the length of the daughter mitochondria on normalized MitoSox intensity before fission (n= 52 fissions). (**f**) Rates of peripheral and midzone fissions in control Cos-7 cells (n=10 fields of view) versus cells treated with 500nM of the ROS scavenger MitoQ (n= 10 fields of view). (**g**) Dependence on the length of the daughter mitochondria of ratio-metric intensity of Grx-roGFP immediately before fission (n= 52 fissions). **h**, Dependence on the

length of the daughter mitochondria of normalized mito-R-Geco intensity before fission (n= 50 fissions). **i**, Dependence on the length of the daughter mitochondria of normalized Cepia3-mt intensity before fission (n= 61 fissions). **j**, Mitochondrial pH before and after a peripheral or midzone fission from SIM movies of Mito-SypHer transfected Cos-7 cells. **k**, Normalized MitoSypHer intensity as a function of relative position of fission, measured immediately before fission (n=53 fissions). **l**, Mitochondrial ROS before and after a peripheral or midzone fission from ratio-metric images of Grx1-roGFP transfected Cos-7 cells. **m**, Ratiometric Grx1-roGFP intensity as a function of relative position of fission, measured immediately before fission (n=52 fissions). **n**, Mitochondrial matrix Ca^{2+} before and after a peripheral or midzone fission from SIM movies of Mito-R-Geco transfected Cos-7 cells. **o**, Normalized Mito-R-Geco intensity as a function of relative position of fission, measured immediately before fission (n=50 fissions). **p**, Mitochondrial matrix Ca^{2+} before and after a peripheral or midzone fission from SIM movies of Cepia3-mt transfected Cos-7 cells. **q**, Normalized Cepia3-mt intensity as a function of relative position of fission, measured immediately before fission (n=61 fissions). In **(a)**, **(k)**, (**m**), (**o**) and (**q**) circles indicate individual measurements; values of binned groups represented as box plots (line: mean, bounds of box: 25th and 75th percentile; whiskers: min/max values). Light blue areas indicate mean intensity in non-dividing mitochondria (±SD). ns > 0.05, ***P<0.001. Number of experiments, statistical tests and exact P-values are provided in Supplementary Table 1. Scale bars are 0.5 μm. Fission sites are indicated by arrowheads.

Extended Data Fig. 3 | Redistribution of mitochondrial DNA and RNA granules. a, Distribution of PicoGreen foci in the small and large daughter mitochondrion derived from peripheral and midzone fission (n=78 fissions). **b**, Normalized TMRE intensity in the small daughter mitochondria from peripheral fissions that contain 0, 1 or 2 nucleoids (n= 20 fissions). **c**, SIM images of mitochondrial RNA granules (MRGs, FASTKD2) before and after fission. **d**, Number of MRGs per μm length as a function of fission position (n=84 fissions). Blue line shows average MRG per length in non-dividing mitochondria (n=41) **e**, Distribution of the number of MRGs (FASTKD2; n=84 fissions) and **f**, replicating nucleoids (mito-Twinkle; n=74 fissions) in smaller (light) and larger (dark) daughter

mitochondria from peripheral (orange) and midzone (green). **g**, Number of BrU positive foci per cell in control Cos-7 cells (n=39) and cells exposed to UV light for 3 min prior to measurement (n=98). **h**, Time-lapse SIM sequence of Cos-7 mitochondria (mito-RFP, grey) and autophagosomes (EGFP-LC3B, green), where the small daughter mitochondrion from a peripheral fission is being taken up by an autophagosome (asterisk). In (**b**) and (**g**) circles indicate individual measurements; line: mean, bounds of box: 25th and 75th percentile; whiskers: min/max values. *P< 0.05, ***P<0.001. Number of experiments, statistical tests and exact P-values are provided in Supplementary Table 1. Scale bar is 0.5 μm.

Extended Data Fig. 4 | Time-course of physiological changes and recruitment of fission regulators. Time course of fluorescent signals in four examples of Cos-7 mitochondria displaying normalized **a**, TMRE intensity and **b**, mito-R-Geco intensity with corresponding SIM images in the mitochondrial compartment giving rise to the smaller daughter mitochondria before a peripheral division. **c**, Average inner membrane diameter at the constriction site at several time-points before fission, measured in mito-R-Geco transfected Cos-7 cells during the time window where Ca^{2+} is elevated (green box in b, n = 10 fission events). **d**, Time course of lysosome co-localization and **e**, autophagosome co-localization at constriction sites for peripheral fissions, by measuring Lamp1-mEGFP and EGFP-LC3B intensity respectively. For EGFP-LC3B measurements, cells were pre-treated with 10 μM CCCP to increase LC3 signals. **f**, Normalized Drp1 intensity at the constriction sites prior to peripheral fission in four examples of Cos-7 mitochondria with corresponding SIM images. Blue dotted lines (t= 0s) marks the timepoint of fission.

Extended Data Fig. 5 | Peripheral and midzone fissions interact differently with the mitochondrial network and the distribution of the fission positions is regulated independently. a, Schematic diagram depicting the fate (”no event”, another “fission” or “fusion”) of each daughter mitochondrion from peripheral and midzone fissions after the initial division in postnatal cardiomyocytes. Only

mitochondria, that could be traced for more than 100 seconds post-fission were included in the analysis. **b**, Distribution of the relative position of in starved Cos-7 cells, with peripheral (1-25%) fission labeled in orange and midzone fissions (25-50%) in green (n=212 fissions). The frequency distribution of Cos-7 control samples is superimposed in grey (replotted from **Fig. 1c**). **c**, Distribution of the relative position of constriction/fission along the length axis of isoproterenol treated mouse cardiomyocyte mitochondria (n=356 fissions) and **d**, miR-199 treated cardiomyocytes (n=225 fissions) respectively. The frequency distribution of untreated mouse cardiomyocytes samples is superimposed in grey (replotted from **Fig. 1e**).

Extended Data Fig. 6 | Peripheral and midzone fissions are both Drp1 mediated but involve distinct upstream mechanisms. a, Two-color SIM images of mitochondria (mito-GFP, greyscale) and Drp1 (Drp1-mCherry, red) undergoing peripheral or midzone fission. **b**, Normalized Drp1 intensity on the constriction sites of peripheral and midzone divisions. The threshold for a Drp1 accumulation (blue dotted line) was set at a signal > 3x over background (n= 107 fissions). **c**, Time-lapse sequence of a SIM movie, where both mitochondrial outer membrane (TOM20-GFP) and inner membrane (mito-RFP) were labeled to detect MDV formation (arrowhead). **d**, Quantification of the fission positions for mitochondria undergoing MDV formation or not before or after division (n= 41 fissions). **e**, SIM images of peripheral and midzone constrictions in fixed Cos7 cells labeled with anti-PDZD8 (red). **f**, Distribution of normalized fluorescent intensities of anti-PDZD8 staining in fixed Cos7 cells for peripheral (orange) and midzone (green) fissions (n= 38 fissions). **g**, Rate of peripheral and midzone fissions in control cells (n= 10 fields of view) versus cells treated with Inf2 siRNA (n= 10 FOV). **h**, Correlated confocal and transmission electron microscopy (CLEM) of mitochondria in Cos-7 cells labeled with Mito-GFP, fixed 24 h after expression. Zoom in of two individual mitochondria with a peripheral (orange frame) and a midzone (green frame) constriction in the TEM plane containing the widest diameter of the constriction site. A pseudo-coloring of three consecutive TEM z-sections recombined into a single rendering shows mitochondria (green) and ER (magenta). Scale bar represents

2 μm in confocal and 200 nm in TEM images. **i**, SIM images of peripheral and midzone constrictions in fixed Cos7 cells labeled with anti-Tom20 (grey) and anti-Mff (green), **k**, anti-Fis1 (red) and **m**, anti-Mid49 (green). **j,** Distribution of normalized fluorescent intensities of anti-Mff (n= 92 fissions), **l**, anti-Fis1 (n= 59 fissions) and **n**, anti-Mid49 (n= 29 fissions) staining in fixed Cos7 cells for peripheral (orange) and midzone (green) fissions. **o**, Normalized Fis1-GFP intensity at the fission site of peripheral (left) and midzone (right) divisions (orange dots: peripheral, green dots: midzone; n= 35 fissions). **p**, Quantification of the peripheral (orange) and midzone (green) fission rates in wild-type (n=16 FOV) and Mff-/-/ Mid49-/-/Mid51-/- tKO (n=16 FOV) MEFs stained with Mitotracker green. **q**, Quantification of the peripheral (orange) and midzone (green) fission rates in control Cos-7 cells and cells treated with siRNAs against Mff or Fis1 (n≥ 13 FOV per group). n.s. P>0.05, ***P<0.001. Number of experiments, statistical tests and exact P-values are provided in Supplementary Table 1. Scale bars are 0.5 μm. Fission sites are indicated by arrowheads.

Extended Data Fig. 7 | Silencing efficiency of Fis1, Mff and Inf2 siRNA in Cos-7 cells. a, Western blot analysis of protein levels for Cos-7 cells 72 h after transfection with two siRNAs against Inf2 at two different concentrations (pmol). Molecular mass is in kilodalton. **b**, Western blot analysis of protein levels for Cos-7 cells 72 h after transfection with 12.5 pmol of siRNA against Fis1 or Mff. **c**, Mean fluorescent intensity in U2OS cells endogenously expressing Mff-GFP or **d**, Fis1-GFP in control conditions and 72 h after transfection with siRNA against Fis1 or Mff (n>39 cells per group). **e**, Relative Mff RNA expression levels in control cardiomyocytes and in cardiomyocytes 48 h after transfection with siMff and with/without Isoproterenol treatment. **f**, Relative Fis1 RNA expression levels in control cardiomyocytes and in cardiomyocytes 48 h after transfection with siFis1 and with/without Isoproterenol (Iso) treatment. n.s. P>0.05, *P< 0.05, **P<0.01, ***P<0.00. Number of experiments, statistical tests and exact P-values are provided in Supplementary Table 1.

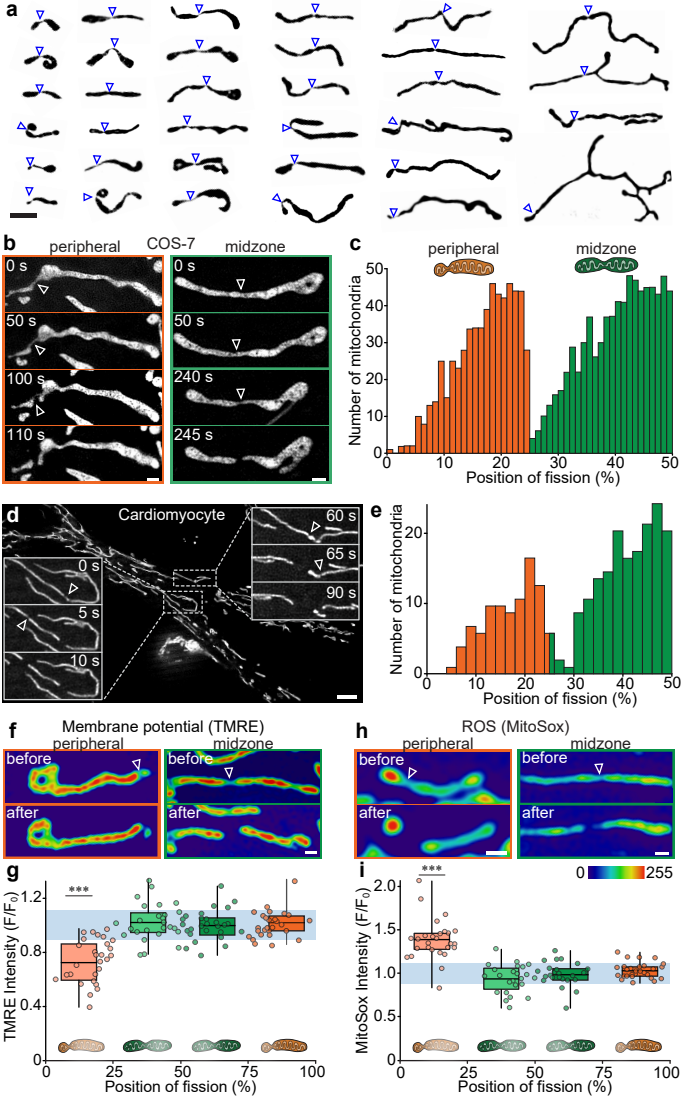
a
b
peripheral
COS-7
midzone
0 s
50 s
100 s
110 s
0 s
50 s
240 s
245 s
c
peripheral
midzone
Number of mitochondria
Position of fission (%)
d
Cardiomyocyte
0 s
5 s
10 s
60 s
65 s
90 s
e
Number of mitochondria
Position of fission (%)
f
Membrane potential (TMRE)
peripheral
midzone
before
after
h
ROS (MitoSox)
peripheral
midzone
before
after
g
***
TMRE Intensity (F/F0)
Position of fission (%)
i
***
0
255
MitoSox Intensity (F/F0)
Position of fission (%)

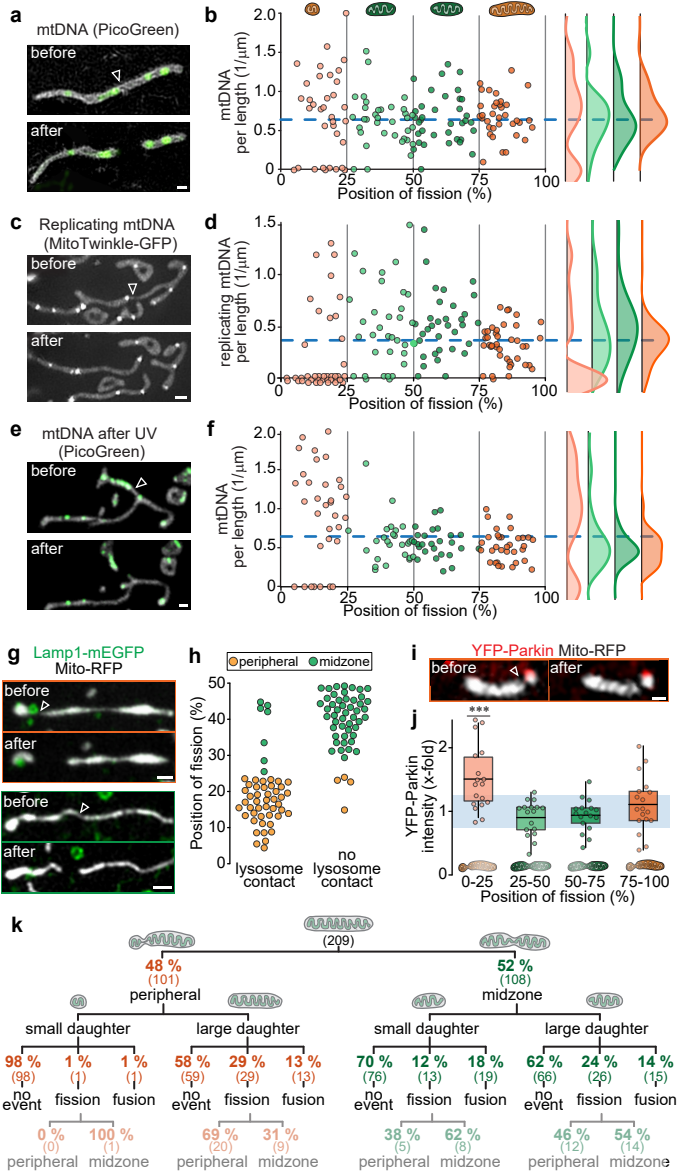
a
mtDNA (PicoGreen)
before
after
b
mtDNA per length (1/µm)
Position of fission (%)
c
Replicating mtDNA (MitoTwinkle-GFP)
before
after
d
replicating mtDNA per length (1/µm)
Position of fission (%)
e
mtDNA after UV (PicoGreen)
before
after
f
mtDNA per length (1/µm)
Position of fission (%)
g
Lamp1-mEGFP
Mito-RFP
before
after
before
after
h
peripheral
midzone
Position of fission (%)
lysosome contact
no lysosome contact
i
YFP-Parkin Mito-RFP
before
after
j
***
YFP-Parkin intensity (x-fold)
0-25
25-50
50-75
75-100
Position of fission (%)
k
(209)
48 % (101) peripheral
52 % (108) midzone
small daughter
large daughter
small daughter
large daughter
98 % (98) no event
1 % (1) fission
1 % (1) fusion
58 % (59) no event
29 % (29) fission
13 % (13) fusion
70 % (76) no event
12 % (13) fission
18 % (19) fusion
62 % (66) no event
24 % (26) fission
14 % (15) fusion
0 % (0) peripheral
100 % (1) midzone
69 % (20) peripheral
31 % (9) midzone
38 % (5) peripheral
62 % (8) midzone
46 % (12) peripheral
54 % (14) midzone

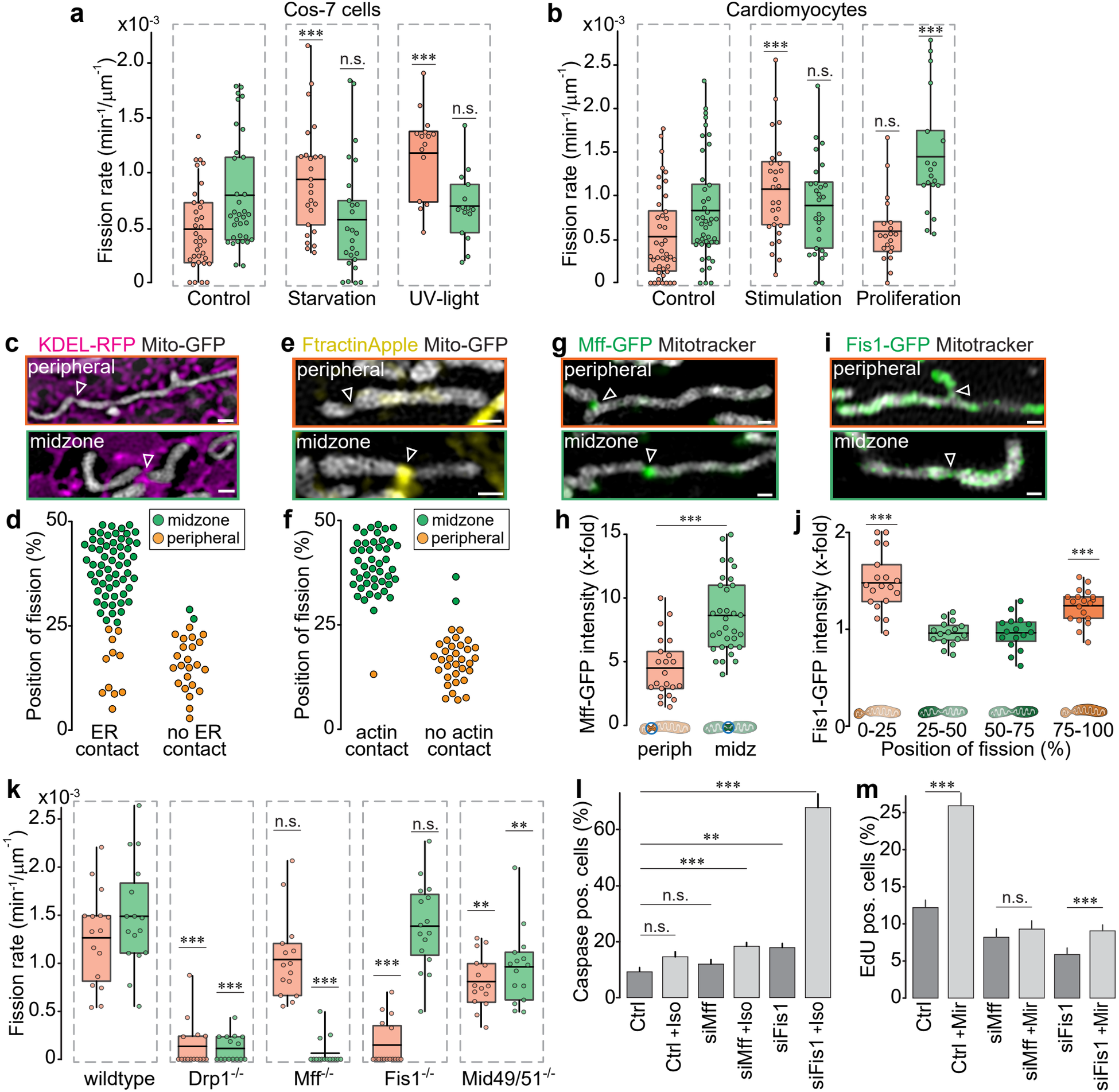
a
Cos-7 cells
x10-3
Fission rate (min-1/µm-1)
2.0
1.5
1.0
0.5
0
***
n.s.
***
n.s.
Control
Starvation
UV-light
b
Cardiomyocytes
x10-3
Fission rate (min-1/µm-1)
2.5
2.0
1.5
1.0
0.5
0
***
n.s.
n.s.
***
Control
Stimulation
Proliferation
c
KDEL-RFP Mito-GFP
peripheral
midzone
e
FtractinApple Mito-GFP
peripheral
midzone
g
Mff-GFP Mitotracker
peripheral
midzone
i
Fis1-GFP Mitotracker
peripheral
midzone
d
Position of fission (%)
50
25
0
midzone
peripheral
ER contact
no ER contact
f
Position of fission (%)
50
25
0
midzone
peripheral
actin contact
no actin contact
h
Mff-GFP intensity (x-fold)
15
10
5
0
***
periph
midz
j
Fis1-GFP intensity (x-fold)
2
1
0
***
***
0-25
25-50
50-75
75-100
Position of fission (%)
k
x10-3
Fission rate (min-1/µm-1)
2.5
2.0
1.5
1.0
0.5
0
***
***
n.s.
***
n.s.
***
**
**
wildtype
Drp1-/-
Mff-/-
Fis1-/-
Mid49/51-/-
l
Caspase pos. cells (%)
60
40
20
0
***
**
***
n.s.
n.s.
Ctrl
Ctrl +Iso
siMff
siMff +Iso
siFis1
siFis1 +Iso
m
EdU pos. cells (%)
25
20
15
10
5
0
***
n.s.
***
Ctrl
Ctrl +Mir
siMff
siMff +Mir
siFis1
siFis1 +Mir